Article type: Full Length Article

High fidelity simulation of ultrafine PM filtration by multiscale fibrous media characterized by a combination of X-ray CT and FIB-SEM

Zhengyuan Pan,[†, ‡, §] Xiaole Zhang,[‡, §] Zhaoxia Sun,[†] Fuze Jiang,[‡, §] Luchan Lin,[‡, §] Yun Liang,[†] Min Tang,[†,] Jing Wang[‡, §, *]*

[†]State Key laboratory of Pulp and Paper Engineering, South China University of Technology, Guangzhou 510640, China
[‡]Institute of Environmental Engineering, ETH Zurich, 8093 Zurich, Switzerland
[§]Advanced Analytical Technologies, Empa, Ueberlandstrasse 129, 8600 Dübendorf, Switzerland

[*] Corresponding authors: Prof. Jing Wang (jing.wang@ifu.baug.ethz.ch)
                          Prof. Min Tang (tangminde@163.com)

(Abstract) Air filtration mechanisms in the composite filter media used in practical applications are important and challenging to understand because the component fibers could have various size scales and morphologies. In this work, a three-dimensional digital model of nanofiber-based filter media was reconstructed for the first time based on the X-ray tomography data for the cellulose substrate and the Focused Ion Beam-Scanning Electron Microscope (FIB-SEM) image analysis for the several microns thick (3.82-7.90 µm) electrospun polyvinylidene fluoride (PVDF) nanofiber membrane. Besides the high-resolution model where the details of the fibrous structures were fully resolved, another low-resolution model with approximated unresolved structures was also established. Filtration simulations utilizing these models were conducted considering the drag force, Brownian diffusion and aerodynamic slip. The simulated filtration efficiencies agreed well with the experiments for particles of 70-400 nm, including

the most penetrating particle size (MPPS, 100-200 nm). Moreover, the structure-resolved models had higher accuracy but higher computational costs, while the unresolved simulations saved much running time but over-predicted the filtration efficiency, especially for smaller particles (<100 nm). Our study presents a comprehensive strategy for investigating the composite filter media with multiscale complex structures using a combination of advanced characterization technologies and modular simulation models.

1. Introduction

The safety and environmental issues have recently attracted broad attention due to the continuously deteriorating environment, air pollution and outbreaks of the respiratory infectious diseases,[1] which drives the investigation of air filtration technology and application.[2] As a recognized cost-effective material to capture the suspended particles in air, fibrous filter media with extensively fiber networks and tortuous interconnected pores have been widely used in air filtration,[3] especially for $PM_{2.5}$ particles which may contain various viruses and bacteria, threatening human health.[4] Fibrous filter media utilize different types of fibers, which can be classified by sources, e.g. natural fibers, synthetic polymer fibers, inorganic/mineral fibers and biofibers. As one of the most rapidly growing technology over the last 20 years, nanofibers have been widely adopted in various air filtration applications due to the superb performance in the interception and inertial impaction regime, and their flexibility to be fabricated from different types of materials.[5-9] However, the thin nanofiber membrane (NFM) often has limited mechanical properties. To achieve balance between the high filtration efficiency and the structural integrity during applications, a nanofiber membrane is usually fabricated as a layer or coating to a micro-scale fiber based substrate e.g. cellulose and spunbond substrate,[10] whereby the nanofiber improves the filtration efficiency and the substrate as the support structure enhances the mechanical properties and enlarges the dust storage space. Therefore, it is important to investigate the structure and filtration mechanisms of these composite filter media which were close to the filters used in practical applications.

The detailed analysis for the structures of multiscale composite filter media is the indispensable

information to better understand their filtration mechanisms. However, the accurate structures are difficult to obtain due to the numerous fibers with various size scales and morphologies. The filter media composed of micro-scale fibers can be measured using the standard techniques e.g. digital volume imaging,[11] magnetic resonance imaging,[12] lab or X-ray tomography.[13-16] A typical lab X-ray computed tomography instrument (CT) has a resolution of 5 μm, and the submicron CT or nano CT could measure down to 0.5 μm.[17] Some synchrotron radiation tomographic microscopy performed at high energy beamline could reach an effective pixel size of about 0.15 μm,[18] but the typical minimum object size should be at least 3 voxel size wide for a quality scan.[19] The above examples indicate that it is hard to completely reconstruct membranes containing fibers below 300 nm by using these standard techniques. Thus, the scanning electron microscope (SEM) is commonly utilized to obtain the key features, including diameter, length, curvature of actual fibers of the nanofiber membranes.[20-24] For composite filter media, Zhang et al. reported a single layer PEO@PAN/PSU composite membrane structure model, reconstructed by using SEM images to obtain the pore structure parameters and the average diameters of PAN and PSU fibers, which were about 270 nm and 1.3 μm, respectively.[25] Zhang et al. studied the particle capture performance of a gradient-structure filter media composed of PSU fiber layer (diameter around 1 μm), PAN fiber layer (diameter around 200 nm) and PA-6 fiber layer (diameter around 20 nm), and a 3D digital structure model was generated with the parameters measured by experiments and SEM images.[26] Dusan et al. built up idealized 3D models for filter media with PVDF nanofibers (dimeter around 100nm) layered on melt blown substrate (diameter around 1μm) based on the fiber features obtained

4

from SEM images.[27] However, the slip effect around the nanofibers was neglected in the flow simulations of these studies, which played an important role in reducing the drag force due to nanofibers on the air flow.[28] Wang et al. used a 2-D structure model representing filter media with a nanofiber layer on a substrate, where the nanofiber layer was assumed as a layer with single-fiber thickness consisting of uniformly distributed circular fibers, and the substrate was simplified as a porous jump boundary ignoring the micro-structure inside it.[29] All of these structure models relied on substantial assumptions. The thickness of the nanofiber membranes was often ignored or derived from empirical equations since the cross-section of the nanofiber membranes could be heavily deformed during the cutting process for SEM images.[30] These idealized models used for nanofiber membranes were insufficient to represent the actual structure of the fibers in substrates, especially the cellulose fibers with hollow structure, where the inner diameter could be different due to the difference in sources and treatment,[31] and thus could compromise the quality of numerical calculations for the filter performance. It is difficult to reconstruct the composite filter media with single characterization method. Moreover, the flow regimes in the substrate and nanofiber membrane were different due to the various fiber scales.[32] It remains unclear whether the slip model used at the surface of the nanofiber in numerical simulations could be suitable for composite filter media.

This work studied the particulate filtration process of nanofiber-based composite media with experimental and simulation methods. The filter media composite #1, #2 and #3 were prepared by electrospinning PVDF nanofibers on the cellulose fiber-based substrate with different fabrication durations, which were 1.0, 1.5 and 2.0h, respectively. The average diameter of

PVDF nanofibers was around 309 nm, and the diameter of the fibers in the substrate was around tens of microns.

The 3D digital structure models of the three nanofiber-based composite filter media were first developed by a new method which combined X-ray tomography and FIB-SEM. The 3D voxel-based virtual substrate and NFMs were respectively created based on the X-ray tomography (CT) slices and the FIB-SEM images analytic data. Then the voxel sizes of the substrate and NFM were unified to be assembled together to obtain the complete composite structures. In addition to the high-resolution model in which the details of the fibrous structures were fully resolved, another low-resolution model with approximated unresolved structures was also established. Particulate filtration simulations based on the resolved and unresolved models were carried out considering the air drag force, Brownian diffusion and slip effect around the surface of fibers. The obtained results from numerical simulations such as pressure drop and filtration efficiency were analyzed and compared with the corresponding experimental data. The strategy forms the basis of a powerful tool for innovative multi-layer composite media design and optimization. The various composite filter media models proposed here can provide reference for further investigation of the dynamic evolution of the microstructure and the macroscopic filtration characteristics of composite filter media in the long-term particle loading process.

2. Experiment

2.1 Material and samples preparation

The substrate composed of micro-scale cellulose and polyester (PET) fibers was prepared with

the wet-laid method, provided by Fibrway (Guangzhou, China). Then a PVDF nanofiber membrane was fabricated on the substrate by electrospinning. For the fabrication of NFM, polyvinylidene fluoride (Mw = 15000, Sigma-Aldrich Co. Ltd) powders were dissolved in N, N-dimethylformamide (DMF)-Acetone (Sigma-Aldrich Co. Ltd) (1:1 *wt*.%), and the solution was stirred for over 12 hours at room temperature. A multi-jet electrospinning machine (NaBond Technologies Co. Ltd.) equipped with three spinnerets and a rotating drum substrate was used to produce the double layer composite filter media. The detailed parameters for the electrospinning process were summarized in **Table 1**.

2.2 Filter media characterization

2.2.1 Fiber size distribution and thickness

The fiber diameter distribution was determined by measuring over 50 fibers in the SEM images using an image analyser (Image J, NIH).[33] Different methods were utilized to characterize the thickness in this study due to the dual-layer structure of the filter media containing fibers with different scales. The thickness of the substrate was directly determined by SEM visualization with normal sampling method. Since the NFM was too weak and thin to keep the cross-section from deforming during the normal cutting process, a combined FIB-SEM (Helios NanoLab DualBeam, USA) was used to measure its thickness. The cross section was exposed by a FIB milling and imaged in SEM secondary electron (SE) mode at a sample tilt of 52 degree. After tilt correction, the thickness of NFM was determined.

2.2.2 Air permeability and solidity

The air pressure drops of the medium were measured at different face velocities from 16.67 to 100 mm/s. Specially, the pressure drop (Δp_{n}) of the NFM was estimated by subtracting the pressure drop of substrate Δp_{s} from the overall pressure drop of composite filter media. A gas pycnometer (Accuoyc II 1340, Micromeritics) based on the gas displacement method was applied to determine the skeleton density of the substrate and the analysis gas was helium. Then the solidity φ can be derived by Equation 1.

$$\varphi = \frac{\rho_t}{\rho_s} \tag{1}$$

where ρ_s was the skeleton density; ρ_t was the macro density of material defined as the ratio between the mass and the total volume of the substrate. Since the solidity of NFMs could not be determined with the gas pycnometer directly, a method by fitting simulated results with measured values was used.[34] Air flow simulations were conducted on the generated 3D virtual nanofiber structures with predefined solidities (the generation and modeling process to be discussed).

2.2.3 Particle collection performance characterization

The experimental setup for filtration efficiency test was shown in **Figure S1**. The monodisperse sodium chloride nanoparticles were utilized in the tests. The dry and clean compressed air was delivered to a lab-made aerosol generator to generate polydisperse sodium chloride particles by atomizing 1 *wt.*% NaCl solution. The generated aerosol went through a diffusion dryer for evaporating the water, and then neutralized by a Kr-85 bi-polar charger to reach the Boltzmann

equilibrium charge distribution. The monodisperse particles with mobility diameters of 50, 70, 90, 100, 200, 300, 400, 500 nm were respectively selected by a differential mobility analyser (DMA, model 3081, TSI). A laminar flow meter was set before DMA to ensure the ratio between the sheath flow and the aerosol flow entering the DMA was around ten. [35] Two condensation particle counters were installed upstream and downstream of the filter holder to measure the particle concentrations. Two mass flow controllers (MFC) were used to keep the aerosol and makeup air flow rates in agreement with the experimental requirement. More details of the setup can be found in the previous work.[36] The filtration efficiency was defined by the percentage of the particle collection as in Equation 2.

$$E_{total} = 1 - \frac{C_{down}}{C_{up}} \tag{2}$$

where C_{down} and C_{up} were respectively the up- and down-stream particle number concentrations.

3. Numerical simulation

3.1 Reconstruction of filter media

3.1.1 substrate model

The top-view and cross-sectional SEM images of substrate was showed in **Figure 1**. The cellulose fibers in the substrate had irregular shapes and hollow structure, often twisted and entangled with each other, which made it difficult to reconstruct the internal micro-structure by using the method to randomly generate fiber structures with only parametric constraints such as mean fiber size and porosity. An X-ray tomography-based method was used to build the

digital structure of the cellulose substrate. **Figure 2** showed the reconstruction processes, including slices acquisition, image processing. Here, the air flow direction was aligned with the z-axis, while the surface of membrane was defined parallel to the x-y plane. The slices acquisition was conducted by using a tomography instrument (RX Solution Easy Tom XL) equipped with 160 kV and 230 kV X-ray sources. The tube with 40 kV was used for electrons striking to produce the X-ray cone beam in this study, and the tube current was 160 µA. Raw X-ray digital images were captured by a high resolution and high-speed CCD detector. The distance between the X-ray source and specimen was 7.10876 mm, and the X-ray source to detector distance was 610.649 mm. The frame rate of the imager was 1 fps. After being filtered by a Tukey window, 1352 slices taken in the vertical (x-z) plane with 1845×1845 voxels were obtained as shown in **Figure 2a,** and the effective voxel size was 1.4785 µm. Then the slices were imported to the processGeo module in the GeoDict software package for 3D processing (**Figure 2b**). The following procedures were utilized to build the 3D digital structure model: 1) permute the axis and rotate the images to align the cross-sections and surface of substrate to the x-z and x-y plane, respectively (**Figure 2c**); 2) crop the slices to 700×700 voxels to avoid the edge effects and cut the domain to 225 voxels with 333 µm thickness according to the measured values (**Figure 2d**); 3) de-noise the images by using the non-local means filter (**Figure 2e-f**); 4) segment the images to separate the pore space from solid (**Figure 2g**). The segmentation was performed by using the single threshold filter. The threshold value was set according to the peak position in the gray value map and the measured solidity. The resulting substrate medium was shown in **Figure 2h**, PET fibers with smooth surface can be distinguished easily from the

cellulose fibers. The domain size was 700 × 700 ×225 voxels, and the voxel length was 1.4785

μm. In contrast to the digital model from CT slices, a random parametric model based on the

component information provided by the producer and fiber orientation from the analysis of

above structure was created, and the other geometric parameters were the same as those of

reconstructed model from CT data. Specially, the hollow structure of the cellulose fibers (see

Figure 1b) was considered by introducing a parameter called the inner diameter fraction,

defined as the ratio of inner diameter to outer diameter of hollow structural section. The inner

diameter fraction was also used as the fitting parameter to match the pressure drop measured in

experiment. The creation process was similar to our previous work (see supporting **Text S1**).[37]

3.1.2 NFM model

Figure 3a-c showed the surfaces of the NFM on top of the composite #1 to #3. The measured

diameters of the PVDF nanofibers were from 0.130 to 0.891 μm. Since the minimum size of

detectable object in the specimen should be 3 times larger than the resolution of CT instrument,

fibers with diameters around 0.1 μm were too small for imaging.[17] Moreover, the PVDF

nanofibers were almost straight and much more regular than cellulose fibers in morphology.

Therefore, a random structure based on the parameters, i.e. fiber size distribution, thickness,

and solidity, was generated to represent the NFM. The log-normal distribution was applied to

simulate the size distribution of nanofibers in the membranes according to the measurements,

and the count median diameter (CMD) and geometric standard deviation (GSD) were 270.65

nm and 1.64, respectively. The cross-sectional SEM images were shown in **Figure 3d-f**, and

the determined thicknesses of the NFM of composite #1 to #3 were 3.82, 6.42 and 7.90 μm,

respectively. It should be noted that the nanofiber model was created based on the assumptions: (a) nanofibers were assumed as straight cylinders; (b) fibers were distributed isotropically in the *x-y* plane and stacked uniformly in the through-plane direction; (c) fibers were allowed to intersect with each other. The sizes of the NFMs of composite #1 to #3 were 700×700×77, 700×700×129 and 700×700×158 voxels, respectively. The voxel size was 50nm. Three repeat structure models were created for each case by changing the random seed to adjust the inner structure.

3.1.3 Composite model

Since the created digital structures, both for substrate and NFM, were voxel-based models, the voxel size of them need to be unified for assembling. To balance the computation cost and simulation accuracy (see **Figure S2**), four substructures with a domain size of 100×100×225 voxels were cut from the reconstructed substrate from CT slices. Then the voxel length of each substructure was refined from 1.4785 μm to 105.607 nm, i.e., each original voxel was divided into 14×14×14 grids. The domain of each substructure was turned into 1400×1400×3150 voxels. The composite filter media were generated by putting the NFM with the same surface area and voxel size on the rescaled substrate. Note that, up to this step, the voxels constituting the virtual fiber structures were considered as solid, and the other voxels were treated as empty, and these digital composite media were noted as resolved models. In contrast, the unresolved composite models were created, where the detailed structure of NFM was ignored and replaced by a porous jump plane composed of porous voxels, which were simplified computational grids representing the average properties of the NFM. The virtual substrates were still from the CT

slices. The porous jump plane was modelled as a homogeneous material with given thickness and permeability from experiments, and the pass-through model (the details to be discussed) was used for describing the probability that a particle passed through the filter media. The domain size of the unresolved model for the entire composite was 700×700×226 voxels, and the voxel size was the same with the reconstructed substrate, which was 1.4785μm.

3.2 Numerical simulation

3.2.1 Air flow

A well-known integrated software package GeoDict (Math2Market, Germany) was used in this study for the air flow and particle filtration process simulations. The fluid inside the virtual structures was assumed viscous, incompressible and steady. Conservation equations of mass (continuity equation) and momentum (Navier-Stokes equation) governing fluid flow in differential form can be given as follows:

$$\nabla \vec{v} = 0 \tag{3}$$

$$\rho(\vec{v} \cdot \nabla \vec{v}) = -\nabla p + \mu \nabla^2 \vec{v} + \vec{f} \tag{4}$$

where ρ is the fluid density, $\vec{v}$ was the flow velocity, p is the pressure, μ was the fluid density, and $\vec{f}$ was a force density. In the case of fibrous filter media considered here, the Reynold number was sufficient small ($Re \ll 1$), the conservation momenta can be simplified into Stokes equation as Equation 5:

$$-\mu \Delta \vec{u} + \nabla p = \vec{f} \tag{5}$$

13

The slip effect around the nanofibers was also considered. In this work, the Knudsen number

(Kn) was 0.21, indicating that the air flow around the nanofibers was mainly in the slip or early

transition flow regime ($0.1 < Kn < 0.4$). Kirsch et al. stated the slip model may be applied up

to $Kn \sim 1$. [38] Thus, the rarefaction effect along the nanofibers could be described as a finite

partial slip using Maxwell's velocity slip as Equation 6.[39]

$$v_w = \frac{2 - \sigma_v}{\sigma_v} \lambda \frac{\partial v}{\partial n} \tag{6}$$

where v_w was the tangential velocity of the flow at the wall, σ_v was the tangential

momentum accommodation coefficient, which was taken as unity here,[24] λ was the mean

free path of air molecules and it was 66 nm, and $\frac{\partial v}{\partial n}$ was the strain rate in the normal direction.

The standard LIR (left-identity-right) solver of Geodict, using a very memory efficient adaptive

grid structure, was employed to solve the partial differential equations describing the fluid

dynamics.[40] The error bound stopping criterion was set to 0.01. The configurations of

boundary conditions were shown in **Figure S3**. Periodic boundary conditions were applied for

the inlet, outlet and boundaries parallel to the flow directions. An implicit in-flow and an out-

flow region were added, which were both 200 voxels thick, to avoid the flow channel closure.

3.2.2 Particle transport

The movement of the particle during the filtration process was simulated by using Lagrangian

Particle Tracking method. The dispersed two-phase flow was assumed to be dilute, i.e. the

distance between the particles in the air was large enough to ignore the particle-particle

collisions, and the flowing particles have no effect on the flow. The sodium chloride particles were simplified into spherical particles, and the motion of each particle was influenced by the combination of the fluid drag force and Brownian motion. Then the trajectory of each particle can be obtained by solving the equations as follows:

$$m\frac{d\vec{u_p}}{dt} = 3\pi\mu\frac{D}{Cc}(\vec{u_a} - \vec{u_p} + \sqrt{\frac{2k_BT}{\gamma}}\frac{d\vec{W}(t)}{dt}) \qquad (7)$$

$$\frac{dx_p}{dt} = u_p \qquad (8)$$

where m was the particle mass (kg), u_a was the air flow velocity (m/s), u_p was the particle velocity (m/s), D was the particle diameter (m), k_B was the Boltzmann constant (J/K), T was the temperature (K), γ was the friction coefficient, dW was 3D Wiener measure ($\surd$ s), responsible for the continuous-time stochastic process. As the diameters of NaCl particles we investigated were down to nanoscale, the slip condition was needed. Cc was the Cunningham slip corrections factor which can be given as Equation 9.[41]

$$Cc = 1 + \frac{\lambda}{D}(2.34 + 1.05e^{-0.39\frac{D}{\lambda}}) \qquad (9)$$

The computation domain and boundary condition configurations for particle transport were the same as those in the air flow simulation. the particle initial position was located in the added inflow region, which was 1 micron downstream from the inlet, to avoid escaping particles across the inlet due to Brownian motion. The diameters of the simulated particle were in the range of 10-1000 nm, and 1000 particles of each diameter were tracked during the filtration

process. For the simulation of resolved models, particles were assumed captured after first touching the fibers both in the NFM and substrate, while for the unresolved composite models, the pass-through model was used for the porous jump NFM and the 'Caught on first touch' collision model was used for solid phases in the substrate. In terms of the pass-through model, whether a particle was captured relied on the pass-through probability of the passed voxel, and the distance covered in these voxels.[42] Thus, the probability $p(l)$ for a particle to travel a distance without getting captured can be written as

$$p(l) = (1\text{-}E_{NL})^{\frac{l}{t_{NL}}} \tag{10}$$

where l was the displacement of the particle, t_{NL} was the thickness of the NFM. The details of configured parameters in the particle filtration simulation were listed in **Table 2**.

4. Results and discussions

4.1 Structure and air flow characteristics

After 3D image data from X-ray CT were converted into the digital structure, the validation of these material models was conducted. The substrate model was characterised and compared to the actual material. **Figure 4a(i)** was the surface SEM image, and the surface morphology of the reconstructed substrate was shown as **Figure 4a(ii)**. Fibers consisting the virtual structure were rendered black and the depth of field was expanded to make more fibers visible. Since the cylindrical PET fibers were easily identified from the cellulose fibers, the diameters of them were determined, and then compared with the measurements from SEM images. The mean diameters of PET fibers in physical and digital structures were respectively 11.05 and 11.09 μm.

The excellent agreement revealed that there was no significant geometric distortion during the reconstruction process. Also, the solidity distributions in the reconstructed substrate were analysed. The solidity of a structure model was defined as the number of voxels counted inside the solid structure to the total voxels in the domain. The solidities on the slices normal to the y direction was shown in **Figure 4b**. The black curve showed the solidity oscillation, while the red part was one of the slices parallel to the y direction. The solidity values fluctuated in the range of 21.5% to 31.20%, and the average value was 26.10%, which agreed well with the measured results (26.63%). The oscillation in solidity could be attributed to the structural heterogeneity of the substrate.[43] **Figure 4c** showed the random parametric substrate model. The red cylinders represented PET fibers, while the curved green and yellow objects with hollow structure represented two types of cellulose fibers in the actual substrate.

Figure 4d compared the measured and simulated pressure drops across the substrate at different face velocities from 16.67 to 100 mm/s. As in the air flow simulation process, the Stokes equation was used to simulate the flow filed, leading to the linear relation between the pressure drop and the surface velocity. The pressure drop from experiments was in agreement with the simulated results. Then the inherent permeability k was derived by applying Darcy's law expressed as Equation 11.

$$v = \frac{-k}{\mu} \frac{\Delta P_s}{t} \tag{11}$$

where v was the face velocity; ΔP_s was the pressure drop; t was the thickness of the media. The permeabilities of the actual filter media, digital model from the CT slices and geometric

parameters were respectively 1.47×10^{-11}, 1.57×10^{-11} and 1.50×10^{-11} m^2. It revealed that the porous structures of digital models were nearly the same with the actual media. **Figure 4e** presented the velocity magnitude inside the digital substrate from CT slices at the flow velocity of 5.35 cm/s. The porous structure inside the substrate formed the flow channels for the air passing through the substrate, and the uneven pore sizes led to the inhomogeneously distributed flow velocities.

Before the simulation of air flow inside the NFMs, the first order Maxwell model used at the surface of fibers were evaluated (see supporting **Text S2** for detailed discussions). The simulated pressure drops with no slip and slip boundary conditions were also compared and showed in **Figure S4c**. As expected, the simulated pressure drops of substrate with slip and no-slip boundary conditions were in good agreement because the *Kn* was close to 0, while the pressure drops across the NFMs using slip boundary condition were much lower than using no-slip boundary condition.

The comparisons of pressure drop vs. face velocity curves of the NFMs from experiments and simulations were shown in **Figure 5a**. Since the input solidity was tuned to fit the pressure drop measurement results, the pressure drops from simulations agreed well with the experimental results. The derived solidity values of the NFMs corresponding to composite #1 to #3 were respectively 4.1 %, 6.25% and 7%. **Figure 5b-d** showed the final 3D digital structures of the NFMs, the thickness of the virtual NFM increased with the electrospinning duration.

4.2 Particle filtration efficiency

The initial filtration efficiencies of the filter media for the sodium chloride particles from 10 to 1000 nm with a face velocity of 5.35 cm/s were simulated using the reconstructed digital structure models (modelling process to be discussed in the experimental section and numerical models), with the same conditions of the experimental tests. **Figure 6a** compared the simulated filtration efficiencies of the substrate models from CT slices and geometric parameters with the experimental results. The trends of the simulated results agreed well with the experimental values. Good agreement was observed for particles smaller than 300 nm, while for particles larger than 300 nm, simulated efficiencies were slightly higher than the experimental values. This discrepancy can be related to ignoring the re-entrainment influence for larger particles in the numerical simulation.[44] The predicted values from parametric substrate models were higher than those from CT slices-based substrate, which may be caused by the insufficient ability of the idealized parametric models to consider the heterogeneity in the actual material.[43] But the parametric models were convenient for the design of the filter media by adjusting the input parameters such as diameter and length of fibers. As shown in **Figure 6b**, the effect of hollow cellulose fibers on the filtration efficiency of substrate was studied. The increase in the inner diameter fraction of cellulose fibers led to the improvement of filtration efficiency. For a fixed solidity, the amount of fibers contained in the structures increased with the increase of inner diameter fraction of fibers, resulting in the increased effective filtration area.

The simulated filtration efficiencies of the NFMs were shown in **Figure 6c** and compared with the corresponding experimental results. The filtration efficiencies of the NFMs from experiments were estimated based on the determined filtration efficiencies of the whole

composite filter media (E_{total}) and the substrate (E_s) using the relation shown as Equation 12 [29]

$$E_{NL} = 1 - \frac{1 - E_{total}}{1 - E_s} \tag{12}$$

The simulated results showed that the filtration efficiencies increased with the electrospinning durations from 1.0 to 2.0 h, which were consistent with the experimental values. As shown in **Figure 6c**, the MMPS of the three NFMs were all in the range of 100-200 nm at face velocity of 5.35 cm/s. For particle sizes in the range of 70-400 nm including the MPPS, the simulated efficiencies agreed well with the measured values. It is also noted that the simulated efficiency curves started to deviate from the measured values when the particle sizes were smaller than 70 nm or lager than 400 nm. The slight over-predictions for the large particle sizes may be related to omission of effects from particle re-entrainment and particle rebound.[45,46] The minor over-predictions at small particle size range could be caused by the assumption of Equation 12 that the NFM and the substrate act independently during the filtration process. Due to the large diffusion coefficients of small particles (<70 nm) and the wide effective range of the diffusion mechanism, the filtration of small particles by the NFM and substrate may not be considered as independent.[29]

The resolved model and unresolved model corresponding to composite #1 were shown in **Figure 7a(i, ii)**, respectively. The NFMs were rendered as red and located on the substrates, which were comprised of gray cellulose fibers. In the resolved composite model, the PVDF nanofiber and pore structure can be clearly observed, while there was no detailed structure inside the NFM for the unresolved cases. The filtration efficiencies of these structures were

simulated separately. The particle movements during the filtration process were tracked and visualization of the captured particles was displayed in **Figure 7a(iii)** and **a(iv)**. It should be noted that the input filtration efficiencies for particles with different diameters used in the porous jump NFMs were from simulated results shown in Figure 6c**.** The sizes of the deposited particles shown in the figures were enlarged for easy visualization. For the composite filter media, most of the sodium chloride particles were captured by the NFM. As the filtration process progressed, part of the particles passing through the NFM deposited continuously on the fibers of substrate. The digital structures and deposited particles distribution of composite #2 and composite #3 can be seen in **Figure S5**. Furthermore, **Figure 7b, c** showed the statistical summary of the number of deposited particles in the three composite filter media as a function of Z-coordinate for resolved and unresolved models, respectively. With longer electrospinning duration, more PVDF nanofibers were stacked on the substrate, leading to the increase in number of particles filtered by the NFM, which meant the improved total filtration efficiency of composite filter media. Then the number of particles passing through the NFM and deposited on the macro-scale fibers decreased (subplots on the right corner). The red curve representing the number of deposited particles in the substrate of composite #1 was higher than the other two cases. The comparison among the filtration efficiencies of the three composite media obtained from experiments and numerical simulation was presented in **Figure 8a-c**, respectively. Consistent with the statistical summary of the total captured particles, the filtration efficiencies of composite #3 were higher than those of composite #2 and composite #1 due to the thicker PVDF nanofiber membrane. The trends of simulated results from both resolved models or

unresolved models were in good agreement with the tested values. In terms of resolved composite models, the simulated filtration efficiency vs. particle diameter curves agreed well with the experimental results for 70-400 nm particles. For large particle size (500 nm) or small particle sizes (<70 nm), the discrepancy appeared. One of the reasons was the accumulation of over-predictions from the NFM and substrate as we mentioned before. Another possible reason can be related to the inhomogeneity at the interface of NFM and substrate. In the early stage of the electrospinning process, the solidities or fiber sizes of the NFM in the gaps and on the surface of macro-scale fibers contained in the substrate could be inhomogeneous. This could cause the over-prediction of simulation results. On the other hand, the simulated efficiencies of the unresolved cases were higher than resolved models, especially for particles with small sizes. That was because in the pass-through model used in the porous jump NFMs, the probability that a particle traveled in the membrane without getting captured was assumed as the set penetration as long as the displacement of this particle equaled the thickness of membrane. However, since the effect of Brownian motion on small particles was strong, the path lengths of these particles would be larger than the thickness, which could lead to the discrepancy. But for unresolved simulations, the computation time were much shorter than resolved simulations (see **Table 3**), which meant it could be an excellent choice for some time-consuming simulation e.g. particle loading process. In addition, the calculated filtration efficiencies by using Equation 12 with the simulated values of NFMs and substrate were compared with the above results from complete composite filter media. The good agreement between them depicted that the total filtration efficiency of the multi-layer filter media could also be evaluated based on the

22

respective efficiencies of each layer, when the simulation for the complete structure was hardly achieved.

5. Conclusion

In this work, the pressure drop and the particle filtration characteristics of dual layer filter media composed of a nanofiber membrane layered on the substrate were investigated with experimental and simulation methods. The composite filter media with three different thicknesses of nanofiber membrane were respectively prepared by fabricating PVDF nanofibers on the substrate with electrospinning method, and then the structure properties (i.e. solidity of substrate, thickness and fiber diameter distribution) and particle filtration performance for sodium chloride particles in the range of 30-500 nm were experimentally investigated. The digital models for the structures of substrate and nanofiber membranes were created separately, and thencombined to form the composite filter media. The digital model of the substrate containing cellulose and PET fibers with dozens of micron diameter was reconstructed from the slices obtained from an X-ray tomography with sub-micron spatial resolution. The solidity, permeability and average PET fiber size of the reconstructed substrate were 26.10%, 1.57e-11m^2 and 11.09 μm, which were in good agreement with the results from experiments. The digital structure model for the nanofiber membrane was generated based on the geometric parameters obtained from the surface and cross-sectional SEM images. Specially, the solidity was configured by fitting the simulated pressure drops at face velocity from 16.67 to 100 mm/s with the measured values. Then the air flow and particle transport simulations of nanofiber membranes, substrate, resolved and unresolved composite structures were separately conducted.

23

The filtration efficiencies of composite filter media were improved by increasing the electrospinning duration. The simulated filtration efficiency vs. particle diameter curves of the composite filter media agreed well with the experimental results for particle diameter in the range from to 70 to 400 nm. For particles with diameters smaller than 70 nm or larger than 400 nm, the simulated efficiencies were slightly higher than measured results. Results from the resolved models showed higher accuracy than the unresolved models. At the same time, the computational times of the resolved cases were much longer than the unresolved cases.

This work explored the feasibility of creating composite filter media containing multi-scale fibers. Based on these generated structures, more studies such as dynamic evolution of the microstructure and the macroscopic filtration characteristics in the long-time particle loading process, the effect of nonuniform charge distribution will be carried out in the future.
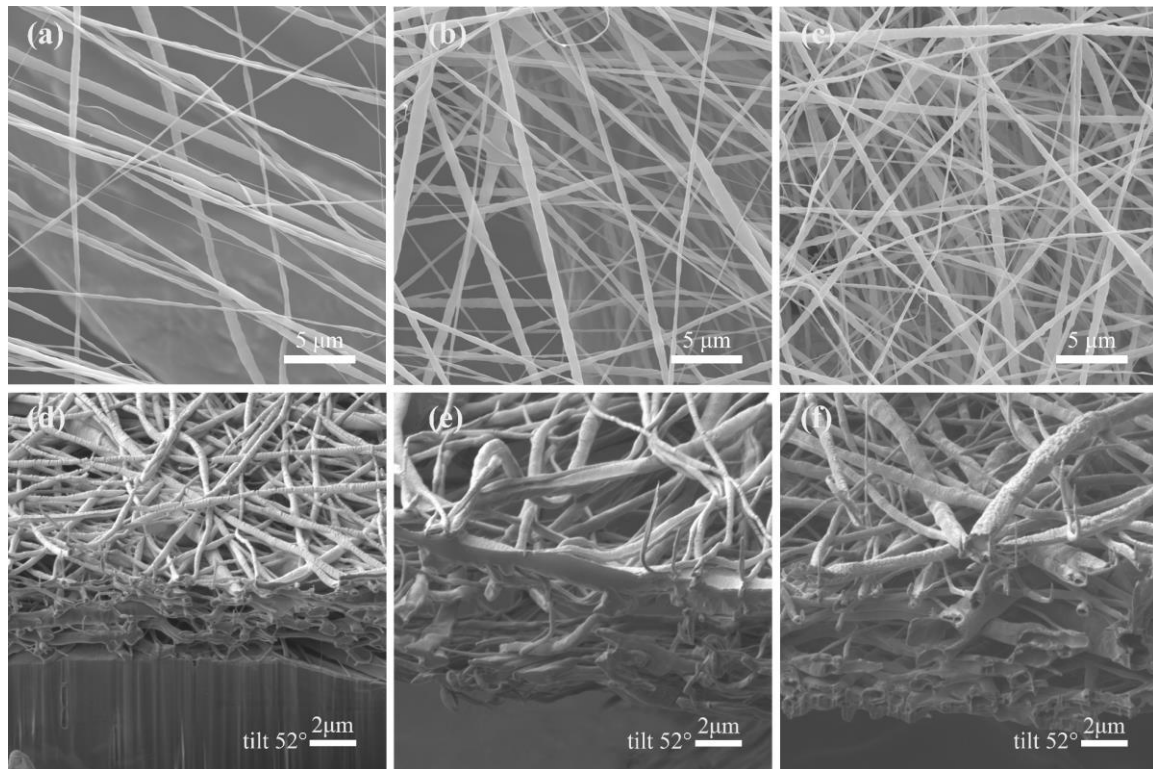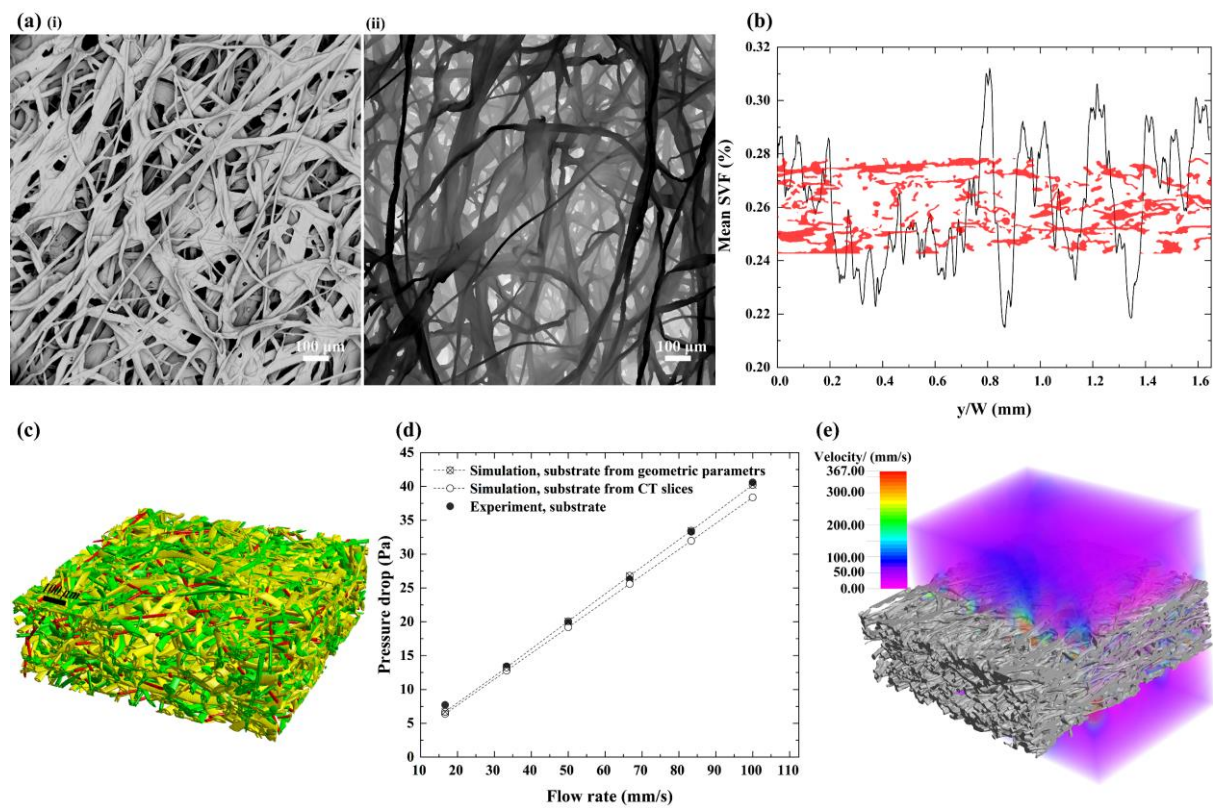
FIGURES
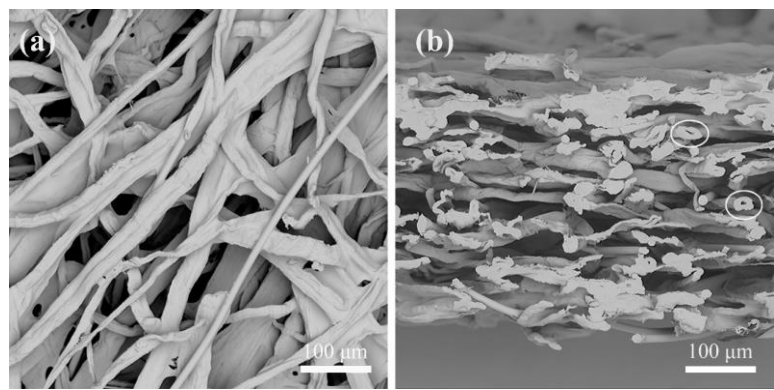
Figure 1. a) Top-view SEM images of substrate, b) cross-sectional SEM images of b).
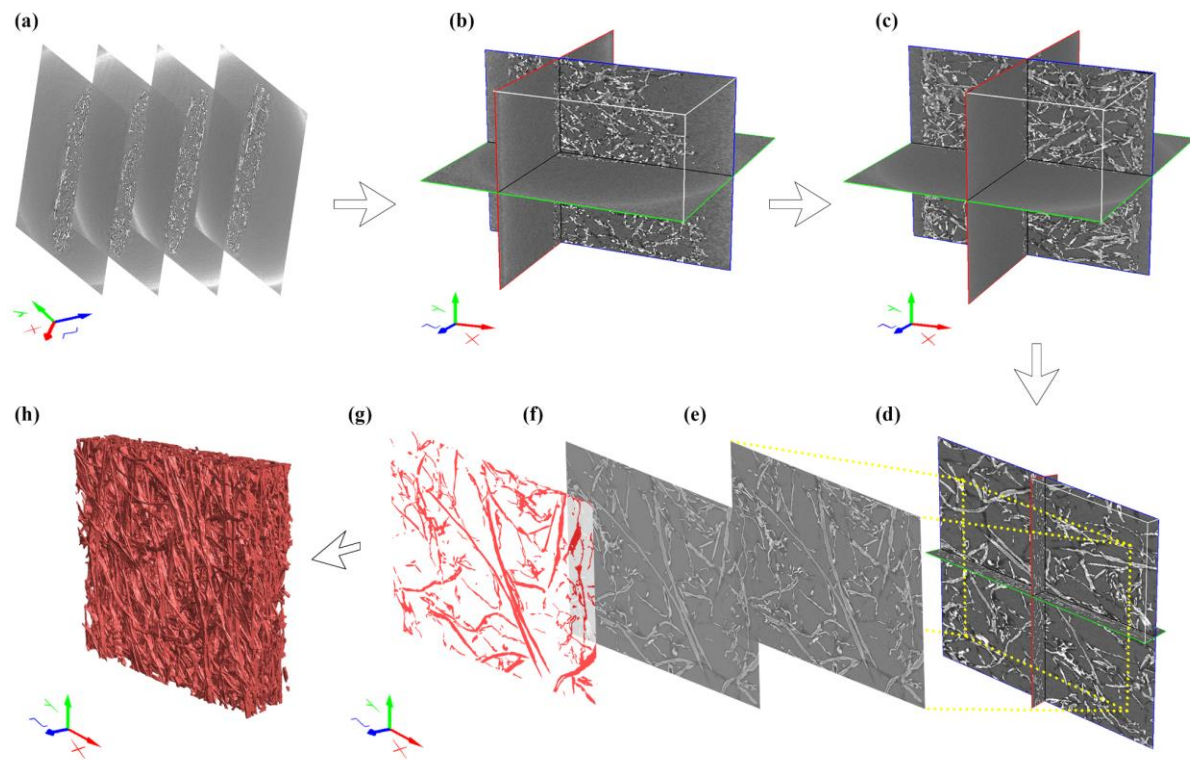
Figure 2. Schematic depicting the steps involved in the reconstruction process of cellulose-based fiber substrate. a) Original slices from the X-ray tomography. b) Import slices for image processing. c) Align to inherent axis of substrate. d) Crop slices into 1000×1000 voxels. e) one of the slices before filtering. f) De-noise slices with non-local means filter. g) Segment slices using the single threshold filter (fibers were rendered to red). h) The final reconstructed virtual substrate.

Figure 3. Top-view SEM images of a) the NFM of Composite #1 (1.0h), b) Composite #2 (1.5h),

c) Composite #3 (2.0h); cross-sectional SEM images of d) the NFM of Composite #1, e)

Composite #2, f) Composite #3.

Figure 4. Verification of virtual cellulose fiber-based substrate. Top–view SEM image of a(i) the substrate medium and a(ii) reconstructed substrate from CT slices. b) SVF distribution of reconstructed substrate from CT slices. c) Virtual substrate generated based on the geometric parameters. d) Measured and simulated pressure drop through the substrate at different flow velocities. e) Velocity field for air flow through the reconstructed substrate from CT slices at a given flow velocity of 5.35 cm/s.
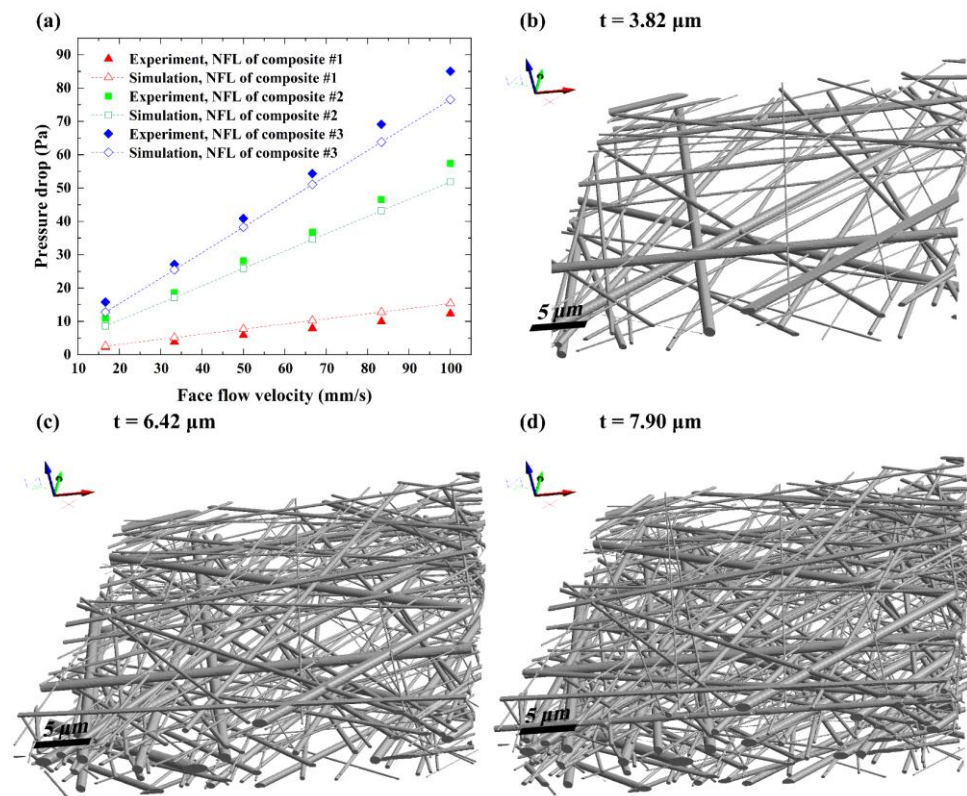
Figure 5. a) Measured and simulated pressure drop through the substrate at different flow velocities. 3D virtual structures of PVDF nanofiber membrane on top of b) composite #1, c) composite #2 and d) composite #3.
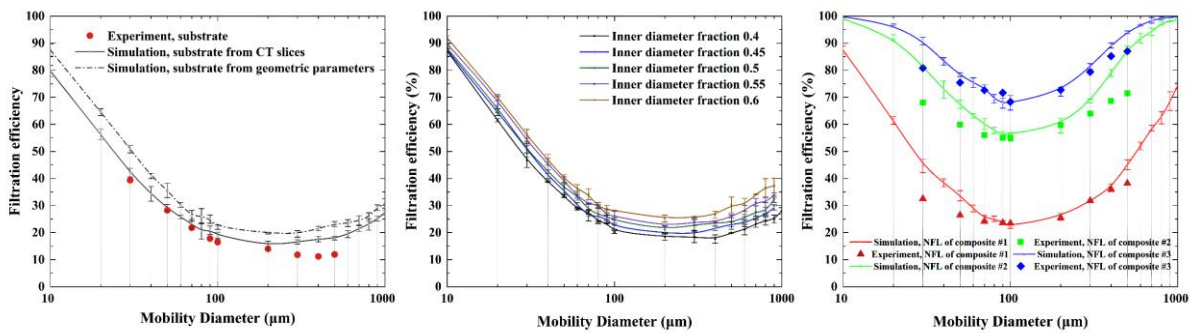
Figure 6. Comparison of filtration efficiencies for particles with different diameters of a) substrate and c) NFM from experiments and numerical simulations. b) Effect of inner diameter fraction of cellulose fiber contained in the substrate on the filtration efficiency.
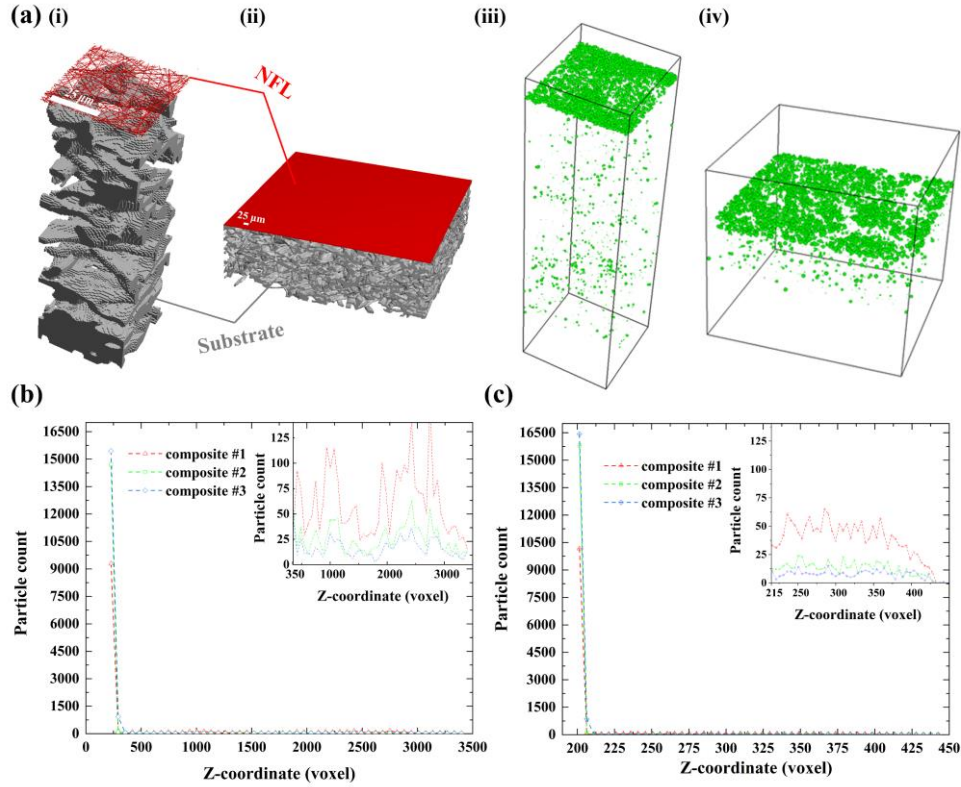
Figure 7. The location and distribution of particles deposited in the computation domain of virtual composite filter media (The NFM, substrate and particles were rendered as red, light gray and green, respectively. a) Visualization of captured particles in the i, iii) resolved and ii, iv) unresolved models of composite #1. The filter media in iii) and iv) were hidden. The count of deposited particles as a function of Z-coordinate for b) resolved and c) unresolved simulations.
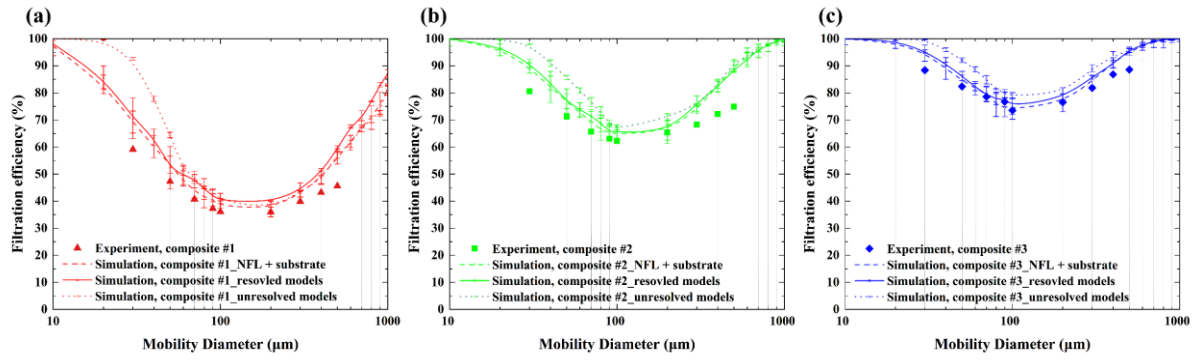
Figure 8. Comparison of filtration efficiencies for particles with different diameters of a) composite #1, b) composite #2 and c) composite #3 from experiments and different numerical simulation methods. The dashed line represented the deduced results from respective efficiencies of NFM and substate. The solid and dotted lines were the simulated results from resolved and unresolved models, respectively.

TABLES

Table 1. Experimental parameters for electrospinning process

Sample	Polymer	Concentration (*wt. %*)	Distance (cm)	Extrusion rate (ml/h)	Times (h)	Voltage (KV)
Composite #1	Polyvinylidene fluoride	14	10	1	1.0	20
Composite #2	Polyvinylidene fluoride	14	10	1	1.5	20
Composite #3	Polyvinylidene fluoride	14	10	1	2.0	20

Table 2. Parameters configured in the particle filtration simulation

Parameter	Values
Air density, $\rho_p / (kg / m^3)$	1.204
Air dynamic viscosity, $\mu / (kg / ms)$	1.834×10^{-5}
Particle density, $\rho_p / (kg / m^3)$	2165
Particle diameter, $D_p / (\mu m)$	0.01-0.1, 0.1-1
Face velocity, $u_0 / (cm / s)$	5.35

Table 3. Computation time for resolved and unresolved composite models

Samples	Time for resolved model (s)	Time for unresoveld models (s)
Composite #1	11983	1387
Composite #2	13636	1055
Composite #3	13890	1157

Supporting Information

Supporting Information is available from the Wiley Online Library or from the author.

Acknowledgements

References

[1] Munster, V. J., Koopmans, M., van Doremalen, N., van Riel, D., & de Wit, E. (2020). A novel coronavirus emerging in China—key questions for impact assessment. *New England Journal of Medicine*, 382(8), 692-694.

[2] Bennett, A. (2010). Air filtration: Innovations in industrial air filtration. *Filtration & Separation*, 47(4), 20-23.

[3] Liu, C., Hsu, P. C., Lee, H. W., Ye, M., Zheng, G., Liu, N., ... & Cui, Y. (2015). Transparent air filter for high-efficiency PM 2.5 capture. *Nature communications*, 6(1), 1-9.

[4] Pope Iii, C. A., Burnett, R. T., Thun, M. J., Calle, E. E., Krewski, D., Ito, K., & Thurston, G. D. (2002). Lung cancer, cardiopulmonary mortality, and long-term exposure to fine particulate air pollution. *Jama*, 287(9), 1132-1141.

[5] Barhate, R. S., & Ramakrishna, S. (2007). Nanofibrous filtering media: filtration problems and solutions from tiny materials. *Journal of membrane science*, 296(1-2), 1-8.

[6] Hassan, M. A., Yeom, B. Y., Wilkie, A., Pourdeyhimi, B., & Khan, S. A. (2013). Fabrication of nanofiber meltblown membranes and their filtration properties. *Journal of membrane science*,

427, 336-344.

[7] Li, J., Zhang, D., Yang, T., Yang, S., Yang, X., & Zhu, H. (2018). Nanofibrous membrane of graphene oxide-in-polyacrylonitrile composite with low filtration resistance for the effective capture of PM2. 5. *Journal of Membrane Science*, 551, 85-92.

[8] Gao, H., He, W., Zhao, Y. B., Opris, D. M., Xu, G., & Wang, J. (2020). Electret mechanisms and kinetics of electrospun nanofiber membranes and lifetime in filtration applications in comparison with corona-charged membranes. *Journal of Membrane Science*, 600, 117879.

[9] Song, J., Zhang, B., Lu, Z., Xin, Z., Liu, T., Wei, W., ... & Li, Y. (2019). Hierarchical Porous Poly (l-lactic acid) Nanofibrous Membrane for Ultrafine Particulate Aerosol Filtration. *ACS applied materials & interfaces*, 11(49), 46261-46268.

[10] Hutten I M (2007) Handbook of nonwoven filter media. In: Composite structure. Elsevire: pp324-325.

[11] Jaganathan, S., Tafreshi, H. V., & Pourdeyhimi, B. (2008). A realistic approach for modeling permeability of fibrous media: 3-D imaging coupled with CFD simulation. *Chemical Engineering Science*, 63(1), 244-252.

[12] Lehmann, M. J., Hardy, E. H., Meyer, J., & Kasper, G. (2005). MRI as a key tool for understanding and modeling the filtration kinetics of fibrous media. *Magnetic resonance imaging*, 23(2), 341-342.

[13] du Roscoat, S. R., Bloch, J. F., & Caulet, P. (2012). A method to quantify the 3D microstructure of fibrous materials containing mineral fillers using X-ray microtomography: application to paper materials. *Journal of Materials Science*, 47(18), 6517-6521.

[14] Lux, J., Ahmadi, A., Gobbé, C., & Delisée, C. (2006). Macroscopic thermal properties of real fibrous materials: Volume averaging method and 3D image analysis. *International Journal of Heat and Mass Transfer*, 49(11-12), 1958-1973.

[15] Schneider, M., Kabel, M., Andrä, H., Lenske, A., Hauptmann, M., Majschak, J. P., ... & Glatt, E. (2016). Thermal fiber orientation tensors for digital paper physics. *International Journal of Solids and Structures*, 100, 234-244.

[16] Viguié, J., Dumont, P. J., Mauret, E., Du Roscoat, S. R., Vacher, P., Desloges, I., & Bloch, J. F. (2011). Analysis of the hygroexpansion of a lignocellulosic fibrous material by digital correlation of images obtained by X-ray synchrotron microtomography: application to a folding box board. *Journal of materials science*, 46(14), 4756-4769.

[17] du Plessis, A., le Roux, S. G., & Guelpa, A. (2016). The CT Scanner Facility at Stellenbosch University: an open access X-ray computed tomography laboratory. *Nuclear Instruments and Methods in Physics Research Section B: Beam Interactions with Materials and Atoms*, 384, 42-49.

[18] Douissard, P. A., Cecilia, A., Rochet, X., Chapel, X., Martin, T., van de Kamp, T., ... & Meinhardt, J. (2012). A versatile indirect detector design for hard X-ray microimaging. *Journal of Instrumentation*, 7(09), P09016.

[19] Du Plessis, A., Yadroitsev, I., Yadroitsava, I., & Le Roux, S. G. (2018). X-ray microcomputed tomography in additive manufacturing: a review of the current technology and applications. *3D Printing and Additive Manufacturing*, 5(3), 227-247.

[20] Cai, R. R., Zhang, L. Z., & Bao, A. B. (2018). PM collection performance of electret filters

electrospun with different dielectric materials-a numerical modeling and experimental study. *Building and Environment*, 131, 210-219.

[21] Zhao, X., Li, Y., Hua, T., Jiang, P., Yin, X., Yu, J., & Ding, B. (2017). Low-resistance dual-purpose air filter releasing negative ions and effectively capturing PM2.5. *ACS applied materials & interfaces*, 9(13), 12054-12063.

[22] Sambaer, W., Zatloukal, M., & Kimmer, D. (2011). 3D modeling of filtration process via polyurethane nanofiber based nonwoven filters prepared by electrospinning process. *Chemical Engineering Science*, 66(4), 613-623.

[23] Rebaï, M., Drolet, F., Vidal, D., Vadeiko, I., & Bertrand, F. (2011). A Lattice Boltzmann approach for predicting the capture efficiency of random fibrous media. *Asia-Pacific Journal of Chemical Engineering*, 6(1), 29-37.

[24] Hosseini, S. A., & Tafreshi, H. V. (2010). Modeling permeability of 3-D nanofiber media in slip flow regime. *Chemical Engineering Science*, 65(6), 2249-2254.

[25] Zhang, S., Liu, H., Yin, X., Yu, J., & Ding, B. (2016). Anti-deformed polyacrylonitrile/polysulfone composite membrane with binary structures for effective air filtration. *ACS applied materials & interfaces*, 8(12), 8086-8095.

[26] Zhang, S., Tang, N., Cao, L., Yin, X., Yu, J., & Ding, B. (2016). Highly integrated polysulfone/polyacrylonitrile/polyamide-6 air filter for multilevel physical sieving airborne particles. *ACS applied materials & interfaces*, 8(42), 29062-29072.

[27] Kimmer, D., Vincent, I., Sambaer, W., Zatloukal, M., & Ondracek, J. (2015, April). The effect of combination electrospun and meltblown filtration materials on their filtration

efficiency. In *AIP Conference Proceedings* (Vol. 1662, No. 1, p. 050001). AIP Publishing LLC.

[28] Li, P., Wang, C., Zhang, Y., & Wei, F. (2014). Air filtration in the free molecular flow regime: a review of high-efficiency particulate air filters based on carbon nanotubes. *Small*, 10(22), 4543-4561.

[29] Wang, J., Kim, S. C., & Pui, D. Y. (2008). Investigation of the figure of merit for filters with a single nanofiber layer on a substrate. *Journal of Aerosol Science*, 39(4), 323-334.

[30] Leung, W. W. F., Hung, C. H., & Yuen, P. T. (2010). Effect of face velocity, nanofiber packing density and thickness on filtration performance of filters with nanofibers coated on a substrate. *Separation and purification technology*, 71(1), 30-37.

[31] Stana-Kleinschek, K., Strnad, S., & Ribitsch, V. (1999). Surface characterization and adsorption abilities of cellulose fibers. *Polymer Engineering & Science*, 39(8), 1412-1424.

[32] Karniadakis, G., Beskok, A., & Aluru, N. (2006). Microflows and nanoflows: fundamentals and simulation (Vol. 29). Springer Science & Business Media: pp16.

[33] Rueden, C. T., Schindelin, J., Hiner, M. C., DeZonia, B. E., Walter, A. E., Arena, E. T., & Eliceiri, K. W. (2017). ImageJ2: ImageJ for the next generation of scientific image data. *BMC bioinformatics*, 18(1), 529.

[34] Ju, W., Jiang, F., Ma, H., Pan, Z., Zhao, Y. B., Pagani, F., ... & Battaglia, C. (2019). Electrocatalytic Reduction of Gaseous CO2 to CO on Sn/Cu-Nanofiber-Based Gas Diffusion Electrodes. *Advanced Energy Materials*, 9(32), 1901514.

[35] Sachinidou, P., Bahk, Y. K., & Wang, J. (2017). An integrative model for the filtration efficiencies in realistic tests with consideration of the filtration velocity profile and challenging

particle size distribution. *Aerosol Science and Technology*, 51(2), 178-187.

[36] Wang, J., & Tronville, P. (2014). Toward standardized test methods to determine the effectiveness of filtration media against airborne nanoparticles. *Journal of nanoparticle research*, 16(6), 2417.

[37] Pan, Z., Liang, Y., Tang, M., Sun, Z., Hu, J., & Wang, J. (2019). Simulation of performance of fibrous filter media composed of cellulose and synthetic fibers. *Cellulose*, 26(12), 7051-7065.

[38] Kirsch, A. A. (1978). The theory of aerosol filtration with fibrous filters. *Fundamentals of aerosol science*.

[39] McNenly, M. J., Gallis, M. A., & Boyd, I. D. (2005). Empirical slip and viscosity model performance for microscale gas flow. *International journal for numerical methods in fluids*, 49(11), 1169-1191.

[40] Linden, S., Wiegmann, A., & Hagen, H. (2015). The LIR space partitioning system applied to the Stokes equations. *Graphical Models*, 82, 58-66.

[41] Allen, M. D., & Raabe, O. G. (1985). Slip correction measurements of spherical solid aerosol particles in an improved Millikan apparatus. *Aerosol Science and Technology*, 4(3), 269-286.

[42] Wiegmann A, Cheng L, Rief S, Latz A, Wagner C, Wersterteiger R (2017). GeoDict user guide. In: FilterDict, pp 8–9. www.geodict.com.

[43] Gong, J., Stewart, M. L., Zelenyuk, A., Strzelec, A., Viswanathan, S., Rothamer, D. A., ... & Rutland, C. J. (2018). Importance of filter's microstructure in dynamic filtration modeling of gasoline particulate filters (GPFs): Inhomogeneous porosity and pore size distribution.

Chemical Engineering Journal, 338, 15-26.

[44] Cleaver, J. W., & Yates, B. (1976). The effect of re-entrainment on particle deposition. *Chemical Engineering Science*, 31(2), 147-151.

[45] Wang, J., Cahyadi, A., Wu, B., Pee, W., Fane, A. G., & Chew, J. W. (2020). The roles of particles in enhancing membrane filtration: A review. *Journal of Membrane Science*, 595, 117570.

[46] Xie, J., Dong, M., & Li, S. (2016). Dynamic impact model of plastic deformation between micro-particles and flat surfaces without adhesion. *Aerosol Science and Technology*, 50(4), 321-330.